LAWRENCE
LIVERMORE
NATIONAL
LABORATORY

UCRL-JRNL-214131

Dynamic force spectroscopy of parallel individual mucin1-antibody bonds

T. A. Sulchek, R. W. Friddle, K. Langry, E. Lau, H. Albrecht, T. Ratto, S. DeNardo, M. E. Colvin, A. Noy

July 29, 2005

Proceedings of the National Academy of Sciences USA

Disclaimer

Classification: Major: BIOLOGICAL SCIENCES Minor: Biophysics

Title:

Dynamic Force Spectroscopy of Parallel Individual Mucin1-Antibody Bonds

Todd A. Sulchek[*], Raymond W. Friddle[*], Kevin Langry[*], Edmond Lau[*], Huguette Albrecht[†], Timothy V. Ratto[*], Sally DeNardo[†], Michael Colvin[‡], and Aleksandr Noy[*,‡,§]

[*] Chemistry and Materials Sciences Directorate, Lawrence Livermore National Laboratory, Livermore, CA, [†] Radiodiagnosis and Therapy, Molecular Cancer Institute, University of California Davis Medical Center, Sacramento, CA, [‡] School of Natural Sciences, University of California, Merced, Merced, CA

[§] To whom correspondence should be addressed. E-mail: noy1@llnl.gov

Mailing Address: L-234, 7000East Avenue, L-234, Livermore, CA 94550

Phone Number 925.424.6203

Fax Number 925.422.3160

Text Pages:

Figure Pages: 6

Table Pages: 1

Word Count in Abstract: 169

Character Count in Manuscript:46,349

Abbreviations: AFM, atomic force microscopy; scFv, single chain variable fragment; MUC1, Mucin1; PEG, poly(ethylene glycol); DFS, dynamic force spectroscopy; NHS, N-hydroxysuccinimyl.

ABSTRACT

We used atomic force microscopy (AFM) to measure the binding forces between Mucin1 (MUC1) peptide and a single chain antibody fragment (scFv) selected from a scFv library screened against MUC1. This binding interaction is central to the design of the molecules for targeted delivery of radioimmunotherapeutic agents for prostate and breast cancer treatment. Our experiments separated the specific binding interaction from non-specific interactions by tethering the antibody and MUC1 molecules to the AFM tip and sample surface with flexible polymer spacers. Rupture force magnitude and elastic characteristics of the spacers allowed identification of the bond rupture events corresponding to different number of interacting proteins. We used dynamic force spectroscopy to estimate the intermolecular potential widths and equivalent thermodynamic off rates for mono-, bi-, and tri-valent interactions. Measured interaction potential parameters agree with the results of molecular docking simulation. Our results demonstrate that an increase of the interaction valency leads to a precipitous decline in the dissociation rate. Binding forces measured for mono and multivalent interactions match the predictions of a Markovian model for the strength of multiple uncorrelated bonds in parallel configuration. Our approach is promising for comparison of the specific effects of molecular modifications as well as for determination of the best configuration of antibody-based multivalent targeting agents.

INTRODUCTION

Interactions between biological molecules drive a vast variety of cellular processes and span a wide range of strength and complexity. Multivalent interactions where several binding units combine to produce superior binding strength are common in both natural and man-made systems, where they play an important role in adaptive immune response (1) and intercellular adhesion (2), as well as in the mechanism of action of many pharmaceuticals (3). Clinical researchers have used multivalency as an affinity-enhancing approach (4, 5) in a variety of immunotherapies and imaging techniques to target specific tissues (6, 7).

Linking several molecules into a large multivalent binding construct also creates bulky agents that exhibit reduced tissue penetration and have a higher probability of accumulation in the liver. Better understanding of the multivalent binding should lead to the creation of more optimal agents that balance binding efficiency and molecular size. Quantitative characterization of multivalent interactions is also important for understanding the basic biophysics of complex molecular systems.

The last decade saw an explosion of interaction force measurement techniques that allowed researchers to measure and apply molecular level stresses (8-10). Atomic Force Microscopy (AFM) allowed researchers to characterize ligand-receptor interactions by simply pulling off the ligand from the receptor using external force (11). Kinetic approaches to the binding force measurements, such as Dynamic Force Spectroscopy (DFS), can quantify kinetic off-rates and the distances to the transition states (12).

We have used DFS to characterize binding of several individual single-chain antibody fragments (scFv) to the Mucin 1 (MUC1) peptide. This interaction is the main

targeting mechanism for a family of experimental radioimmunotherapeutics for cancer treatment, that consist of several antibody fragments on a poly(ethylene glycol) (PEG) scaffold that preloads onto the cancer cells and then catches a subsequently administered radioactive Y^{90} payload (Figure 1A) (13). MUC1 is a large transmembrane glycoprotein which is commonly expressed in variety of epithelial tissues in the human body (14, 15) where it hydrates the epithelia, enhances adhesion to neighboring cells, and provides a barrier to pathogenic invasion. Overexpression of MUC1 with reduced glycosylation is characteristic for prostate, breast, colon, lung, gastric and pancreatic cancers (16, 17)(18) and clinical trials targeting the MUC1 marker in solid tumors with multivalent antibody-based drugs have produced promising results for metastatic breast and prostate cancers (19, 20).

Our experiments recreated the targeting unit of the drug by tethering one or several scFv antibodies to the AFM tip. We have obtained the force spectra for the antibody interactions with the MUC1 peptide immobilized on the sample surface and determined kinetic off-rates and interaction potential widths for individual mono, di, and trivalent interactions. Increase in the interaction valency leads to the precipitous drop in the kinetic off-rate of complex dissociation. Moreover, the experimental data show a remarkable agreement with the Markovian model for uncorrelated rupture of individual parallel molecular bonds.

MATERIALS AND METHODS

Details are given in *Supporting Materials and Methods* which are published as supporting information on the PNAS web site.

Preparation of the MUC1 peptide and scFv antibody. The scFvs used for the measurements as well as for *in vivo* targeting (21) were screened against the synthesized MUC1 peptide core, which consists of the 20-amino acid tandem repeat sequence, PDTRPAPGSTAPPAHGVTSA (22). Five repeats of this sequence, for a total of 100 amino acids, were obtained from the Peptide Synthesis Facility, at University of Pittsburgh (23). The scFvs for this experiment were produced in *E. coli* HB2151 strain. ScFv clones selected from an anti-MUC1 phage display library (21) were expressed with an additional cysteine tag that was engineered into the vector for the addition of a free cysteine linker at the C-terminus, which does not interfere with the binding domain (24).

Functionalization of the AFM tips and substrates. The antiMUC1 scFvs were covalently linked to the surface of the cantilever tip via bifunctional poly(ethylene glycol) (PEG) linkers (Nektar Therapeutics, Huntsville, AL) as shown schematically on the Figure 1B. Commercial model NP silicon nitride AFM cantilevers (Veeco, Santa Barbara, CA) were coated on the tip side with a thin layer of gold (750 Å with 50 Å chromium adhesion underlayer), cleaned with a piranha etch (70% concentrated sulfuric acid and 30% hydrogen peroxide solution), rinsed, and then incubated in 1 mM cystamine solution for 30 minutes to form an amine-terminated self assembled monolayer (SAM).

The amine surface was then treated with two types of bifunctional PEG linkers, capped with either N-hydroxysuccinimyl (NHS) and methoxy (OMe) groups or NHS and maleimide (Mal) groups. We used a 50:1 molar ratio of 10 mM NHS-PEG(2000)-OMe and 0.2 mM NHS-PEG(3400)-Mal in dry chloroform to create low surface density of maleimide groups. Finally, we incubated the tips of the cantilevers in 20 μL of scFv

solution (2.5 mg/mL concentration, pH 7) for 30 minutes to link the free thiol group on the antibody to the AFM tip.

The dilution ratio is critical for controlling the final density of the functional tethered molecules on the AFM tip, and we typically used a 50:1 dilution ratio which resulted in ~10% probability of obtaining one to several individual tethers attached to the AFM tip. In order to increase the frequency of multivalent interactions, several measurements were made at a dilution ratio of 30:1.

Gold surfaces prepared by evaporation of gold onto a silicon substrates, were functionalized with the MUC1 peptide using the same tethering scheme used for the AFM tips. Since the only free amine group on the MUC1 peptide is at the N-terminus, we used this group to link the peptide to the tether. We mixed homobifunctional PEG with NHS groups on each end with the short NHS-PEG(2000)-OMe molecules that provided surface passivation in a 1:50 ratio. MUC1 solution (10 mM in pH 8 buffer) was incubated with the sample for 30 minutes and then rinsed off with pure buffer.

Force spectroscopy. All force measurements used a Nanoscope IIIa AFM (Veeco, Santa Barbara, CA) in force calibration mode. Measurements were performed at 0.5-3 Hz frequencies. A relative trigger of 7nm was used on all force-distance curves to limit both the tip-sample repulsive force and the tip-surface contact area. In addition, upon activation of the trigger, the tip was held at the sample surface for 0.4 s to allow the tethered scFvs to form bonds with tethered MUC1 peptide. All measurements were carried out in 20mM phosphate buffered saline and 100 mM NaCl.

Cantilever spring constants were calibrated with the FFT spectrum analyzer (Stanford Research Systems SR760) using the thermal noise method (25). Rupture traces

were analyzed using Igor Pro 5.0 (WaveMetrics, Lake Oswego, Oregon) and a custom-written set of procedures. Laser optical interference at 635nm was filtered by removing its spectral component from the force signal. We collected the cantilever deflection data at 14 kHz acquisition rate to visualize multiple rupture events occurring in close succession. Before the rupture force determination, RMS force noise was reduced by low-pass filtering the force signal immediately before and after rupture.

For quantitative analysis of the tether stretching, all single bond rupture events were fit by an extended freely jointed chain (FJC) model with parameters determined by Oesterhelt et al (26), with the only fitting parameter being the tether contour length. For multiple tether stretches, we allowed the best fit to determine persistence length and extensibility.

Homology modeling of CD5 scFv and docking of MUC1. The amino acid sequence of the CD5 antibody is 75% identical to the single chain Fv antibody molecule MFE-23 (PDB entry 1QOK) (27), a level of homology that strongly suggests that their three-dimensional structures will be quite similar as well. The sequence alignment between these two proteins was performed using CLUSTALW (28). Three-dimensional models were generated automatically from the alignment described above with MODELLER (29). The linker joining the V_H and V_L regions of the antibody was not present in the crystal structure and was not generated for the homology models of CD5. The quality of the models was evaluated using ProsaII (30). The model with the lowest ProsaII score was used for docking studies.

The MUC1 peptide region containing the epitope (SAPDTRPAP) of breast tumor-specific antibody SM3 defined by crystal structure analysis (PDB entry 1SM3) (31) was

docked onto the surface of the CD5 model using the program Autodock 3.05 (32). Although the epitope recognized by the CD5 antibody has not been determined, the modeled MUC1 peptide fragment contains the highly immunogenic core peptide sequence PDTRP. This sequence contains the epitope for many MUC1 specific antibodies (33).

Kollman-united atom charges were used for the antibody and the MUC1 fragment (34). A 90 × 80 × 80 grid was used for docking with a spacing of 0.375 Å and centered in the hypervariable loops of the antibody. The backbone of the MUC1 fragment was fixed and only the side chains of the peptide were allowed to change. A Lamarckian algorithm was used to generate ligand conformations with the active site (32). The parameters used for the Lamarckian genetic algorithm were the same as in Legge *et al.* except the maximum number of energy evaluations was 250,000 (35). A total of 500 conformers were generated for MUC1 onto the CD5 model. The conformers were clustered using a 2.0 Å RMSD.

RESULTS AND DISCUSSION

Binding system architecture. We have designed our experimental system to minimize the impact of non-specific interactions and to maximize the probability of detecting specific peptide-antibody interactions. An effective approach for discriminating between specific and non-specific forces involves attaching the interacting molecules to flexible polymer tethers (36, 37). The tethers spatially isolate non-specific probe-sample interactions from the specific interactions of the tethered molecules and allow researchers

to discriminate between rupture events using *both* the rupture location and binding force values.

For our experiments we chose to use 30±10 nm-long PEG tethers (Figure 1B) to mimic the architecture of the MUC1-targeting immunotherapy drugs (compare Figure 1A and 1B), as well as to simplify the assignment of the specific rupture events. Note that the length of our tethers was much larger than the PEG persistence length (38); therefore these tethers remain truly flexible, allowing the necessary conformational freedom to maximize the efficiency of the MUC1-antibody interactions. To maximize the probability of observing discrete individual interactions we diluted the active tethers on the AFM probe with the inactive spacer, while keeping high surface density of the MUC1 target. This strategy resulted in about 10% probability of specific interaction detection in our experiments.

Binding force measurements. A typical force vs. separation trace obtained in our measurements showed complicated structure (Figure 1C). As the cantilever pulled away from the surface it passed through several regions corresponding to rupture of different interaction types. After the probe left the tip-sample repulsive contact region (**I**), it entered the first of the attractive interaction regions (**II**). This region in the 10-25 nm range corresponds to non-specific tip-sample interaction. A second attractive interaction region distinguished by a characteristic tether stretching shape (region **III**) corresponds to the interactions of the tethered molecules with the sample surface or with each other. This is the region where we expected to observe the specific interaction of the tethered antibodies and MUC1 peptide, which should be clustered at around two tether length

rupture distance. In the region **IV** the cantilever completely separated from the sample surface and returned to its equilibrium deflection.

To identify specific MUC1-antibody interactions, we have compiled histograms of the rupture forces that occur at one and two tether lengths (Figure 2A). Distributions of the rupture forces below 125 pN were very similar for both tether lengths. In contrast, the force distribution observed at two tether lengths separation showed a distinct peak centered at 150 pN, which was absent in the force distribution observed for one tether length separation. This peak corresponds to the specific MUC1-antibody interactions, while the forces below 125 pN at both one and two tether lengths likely originate from different non-specific interactions between the proteins and the PEG tethers.

Blocking of specific interactions in a competition assay. To verify that the observed peak at 150 pN is due to specific MUC1-antibody binding, we have blocked the specific MUC1-antibody interactions by adding excess of free MUC1 antigen to the buffer solution. Histograms of the rupture forces measured at two tether lengths for blocked and unblocked interactions (Figure 2B) showed that addition of the excess free MUC1 suppresses only the interactions that occur at two tether length and above 125pN, which confirms our assignment of the specific interactions.

Dynamic force spectroscopy of tethered systems. Despite the conceptual simplicity of force spectroscopy measurements, their quantitative interpretation is not straightforward. The relationship between the experimentally-measured bond rupture forces and the interaction potential is described by a kinetic model first proposed by Bell and then developed by Evans (39-41). Exponential amplification of the bond dissociation rate by

the external loading force in the AFM measurement produces a characteristic proportionality of the rupture force, F, to the logarithm of the loading rate, r:

$$F = \frac{k_B T}{\chi_\beta} \ln\left(\frac{r\chi_\beta}{k_{off} k_B T}\right), \qquad \text{(Eq. 1)}$$

where χ_β is the distance to the transition state and the k_{off} is the kinetic off-rate for the bond. Flexible tethers introduce an additional complication to this picture, since they form highly non-linear springs connected in series with the Hookean cantilever spring; fortunately, Gaub and colleagues showed (42) that the Eq. 1 is still valid for tethered systems if we replace the nominal loading rate with the instantaneous loading rate provided by the slope of the tether extension curve close to the rupture event. This approximation, which is valid at fast loading rates is valid for our experiments since the nominal loading rates were over two orders of magnitude above the thermal velocity, that defines the threshold for fast loading (43).

Dynamic force spectroscopy of single MUC1-scFv bonds. To determine the interaction parameters for the single MUC1-scFv bond we used the stretching region of the force vs. extension traces preceding rupture (Figure 1C and 3A) with the PEG chain elasticity model (26). Close fit of the model to the experimental data indicates that the observed traces indeed correspond to the rupture of a single pair of interacting molecules connected to the surfaces of tip and sample by single PEG tethers. When we plotted the measured rupture forces as a function of the logarithm of the instantaneous loading rate determined from the PEG elasticity fits, we have obtained the dynamic force spectrum (Figure 3D, red squares) showing the typical linear behavior predicted by the Eq. 1. This dynamic force spectrum indicates that the unbinding events observed in our experiments

correspond to a single sharp potential energy barrier located at 2.8±0.2 Å (as determined from the fit of the experimental data to the Eq. 1). The value of $2.6 \cdot 10^{-3}$ s^{-1} for the thermal off-rate determined from the dynamic force spectrum is slightly faster than the value of $0.4 \cdot 10^{-3}$ s^{-1} measured in bulk surface plasmon resonance (SPR) measurements (data not shown). However, the SPR measurement included a contribution from antibody dimers; therefore a higher measured off-rate is not surprising.

Stepwise rupture of MUC1-scFv bonds. Close examination of some traces collected at high data acquisition rates revealed that they consisted of stepwise rupture of two bonds in quick succession (Figure 3B,C). We ruled out attachment of multiple antibodies to the same tether since the antibodies contained only a single cysteine residue available for conjugation. Therefore we conclude that the first rupture event on the Figure 3B,C must involve stretching of multiple tethers. Indeed the tether stretching trace before the first rupture showed a larger elasticity and smaller persistence length matching the parameters expected for two PEG tethers (Figure 3B,C). In the situation when the cantilever stretches two tethers connected in parallel we expect the load to be shared by the two bonds (44). Therefore, the effective loading rate applied to each bond will be half of the nominal loading rate. If we use this assumption to normalize the loading rates, we obtain the dynamic force spectrum for stepwise rupture that is identical to the dynamic force spectrum obtained for the rupture of single MUC1-antibody bonds (Figure 3D). Indeed, the linear fit parameters for both spectra are identical towithin the fit margin of error (see Table 1).

Rupture of multiple MUC1-antibody bonds. Roughly 10% of all specific rupture events occurred at forces much higher than the forces for single bond rupture events. We

have found consistently that tether stretching traces preceding these events is fit best by a FJC model consistent with stretching multiple PEG tethers. This fit provided an additional means to estimate the number of the individual protein-antibody pair for each rupture. The same procedure that we used for analysis of stepwise rupture events produced the dynamic force spectra for two- and three-tether ruptures shown on the Figure 4A. Remarkably, a comparison of the force spectra for rupture of one, two and three bonds shows that they exhibit very similar slopes (Figure 4A and Table 1), which correspond to a similar distance to the transition state. We have also determined the effective kinetic off-rates for mono and multivalent MUC1-antibody interactions by fitting the spectra to the Eq. 1 (Table 1). As expected, the off-rates drop precipitously with an increase in the number of bonds. These data clearly illustrate that the main benefit of multivalent interactions is *the reduction on the kinetic off-rate and the corresponding increase in the bond lifetime*. The half life for the common radioactive payload Y^{90} is 65 hours and an ideal multivalent targeting molecule should remain bound to the tumor site for at least this amount of time. Therefore, these results suggest that an effective MUC1-targeting immunotherapeutic should link three scFv units to achieve the necessary binding efficiency.

It is also useful to compare the experimentally measured spread in the rupture force values with the model predictions. Numerical simulations showed that deviations in the normalized rupture force F at high loading rates scale as the number of bonds N (45). Indeed, the histograms of experimental data residuals from the best fits for one, two, and three bonds fit well the Gaussian distributions with the width $N \cdot \sigma$, where σ is the residual

standard deviation from the one bond case (Figure 4B-D). This comparison provides an additional validation for the parallel uncorrelated bond rupture model predictions.

Theoretical description of failure of multiple parallel bonds under load. Our experimental system represents one of the three basic configurations for multiple bond attachments (46): parallel attachment where the load is shared between all the bonds (the other two configurations are the serial connection where all bonds experience the same load (47); and a "zipper" connection, where only one of the bonds experiences the loading force at any given time). In addition to the connection architecture, rupture dynamics of the multiple bonds also depends on the failure mode. In the correlated mode all bonds are closely coupled and failure of one bond implies failure of the rest of the bonds. In the uncorrelated system all attachments can fail independently and the load force is redistributed among the surviving bonds. Quantitative analysis under a correlated bond failure assumption shows that our measured kinetic off-rates would result in an unreasonably low value of the energy barrier of $6.5 \cdot k_B T$. This result is not surprising, since correlated rupture requires close mechanical coupling between individual bonds (46), which the long tethers used in our study cannot provide.

The uncorrelated failure mode implies no particular mechanical coupling between individual bonds (45, 48, 49). Williams showed that the force-induced rupture of the multiple uncorrelated bonds could be described as a Markovian sequence and used numerical simulations as well as analytical approximations to predict the dynamic force spectra for this process (45). He also showed that although the kinetic equations for the uncorrelated parallel bond rupture cannot be solved analytically, a numerical solution and a useful analytical approximation exist. To simplify the description we will use the

normalization for force and loading rate suggested by Evans and Williams in a later publication (46):

$$F = \frac{f}{f_\beta}; \qquad R = \frac{r_f}{f_\beta k_{off}}; \qquad \text{(Eq. 2)}$$

where f_β is the thermal force scale defined as k_BT/χ_β.. The equivalent single bond approximation (45, 46) then produces the following expression relating the normalized loading rate, R, to the most probable rupture force, F^*, and the number of bonds, N:

$$R = \left[\sum_{n=1}^{N} \frac{1}{n^2} \exp\left(-\frac{F^*}{n} \right) \right]^{-1} \qquad \text{(Eq. 3)}$$

To test the model predictions, we have compared our experimental data normalized according to the Eq. 3 with the most probable rupture forces calculated using Eq.4 (we did not use the full set of master equations for the multibond system (45) because we found that Eq.4 produces very close results for our loading regime). The calculated rupture forces fit our experimental data extremely well (Figure 5). We stress that we did not use any fitting parameters to generate the theoretical curves on the Figure 6B; therefore, the Markovian model (45) provides an accurate description of the dynamics of the failure of multiple uncorrelated parallel connections. To our knowledge, this is the first experimental test of this model in a parallel bond system.

MUC1 docking simulations. For an additional validation of the force spectroscopy results, we have compared the measured distance to the transition state with the results of molecular docking of the MUC1 fragment onto the hypervariable loops (antigen binding region) of the homology model of our antibody. The docking simulation shows that the dominant contribution to the bond formed between the MUC1 fragment and the antibody is a slightly buried salt bridge between the residues Arg103 in the scFv and Asp in MUC1

(Figure 6A). In the docked conformation the Asp residue of the MUC1 peptide is 2.6 Å away from the NH group of the ARG103 residue on the antibody (Figure 6B,C). Although only one carboxylate oxygen (OD2) of Asp from MUC1 is interacting with Arg103, a slight rearrangement of the arginine sidechain or a change in the MUC1 backbone would likely allow the second carboxylate oxygen (OD1) of Asp to interact with Arg103. An alternative interaction between the imidazole nitrogen (NE2) of His35 and OD1 of the Asp (2.7 Å separation) is also possible. In either case, two strong interactions dominated by a buried salt bridge formation can form between the Asp residue of MUC1 and the antibody. Potential mean force calculations for similar salt bridge formations show bond widths that range from 2.2 Å to 3.0 Å (50, 51) which compare well with the characteristic rupture distance of 2.8 Å measured in the force spectroscopy experiments.

CONCLUSIONS.

We have used atomic force microscopy to characterize interactions of MUC1 peptide with the scFv antibody in both mono- and multivalent configurations. Long flexible tethers used for attaching the interacting molecules to the AFM tip and samples surfaces allowed us to identify specific binding interactions and separate them from the non-specific interactions. We used instantaneous loading rate values obtained from the fits of the tether elasticity curves to construct accurate dynamic force spectra for the rupture of mono and multivalent MUC1-antibody interactions and to quantify the advantages of the multivalent binding. Each additional MUC1-antibody interaction preserves the force scale for a single interaction, but leads to a precipitous drop in the effective kinetic off-

rate. Moreover, measured dynamic force spectra show excellent agreement with the Markovian model for the rupture of multiple uncorrelated molecular bonds, providing a solid experimental corroboration for the theoretical predictions.

We believe that these results open up significant new opportunities for researchers in areas ranging from biophysics to drug design. Tethered ligand systems can serve as a flexible and versatile model for studying fundamental dynamics of individual bond rupture in biological systems. Multivalent binding is a common tool for molecular targeting that enables extended and more accurate delivery of drugs and molecular labels to specific tissues. We showed that dynamic force spectroscopy can provide an accurate measurement of the kinetic off-rates in molecular systems. These off-rates are the main determinant of the efficiency of the drugs and quantification of the advantages of multivalent binding can provide a valuable input into the design efforts. Finally, researchers can use force spectroscopy experiments similar to what we described to get detailed information about the binding efficiency of different configurations of multivalent binders, which should help to determine optimal configurations for such agents. These results should assist the efforts to design the next generation of superior multivalent drugs and molecular labels.

ACKNOWLEDGEMENTS

This work was performed under the auspices of the U.S. Department of Energy by the University of California, Lawrence Livermore National Laboratory under Contract W-7405-Eng-48 and was supported in part by an LLNL LDRD grant and NCI CA47829 grants.

REFERENCES.

1. Cochran, J. R., Cameron, T. O., Stone, J. D., Lubetsky, J. B. & Stern, L. J. (2001) *J. Biol. Chem.* **276,** 28068-28074.
2. van Kooyk, Y. & Figdor, C. G. (2000) *Curr. Opin. Cell Biol.* **12,** 542-547.
3. Mammen, M., Choi, S. K. & Whitesides, G. M. (1998) *Angew. Chem. Int. Ed. Engl.* **37,** 2755-2794.
4. Holliger, P., Prospero, T. & Winter, G. (1993) *Proc. Nat. Acad. Sci. USA* **90,** 6444-6448.
5. Todorovska, A., Roovers, R. C., Dolezal, O., Kortt, A. A., Hoogenboom, H. R. & Hudson, P. J. (2001) *J. Immunol. Meth.* **248,** 47-66.
6. Souriau, C. & Hudson, P. J. (2003) *Expert Opin. Biol. Theor.* **3,** 305-18.
7. Rowland, G., O'Neill, G. & Davies, D. (1975) *Nature* **255,** 487-488.
8. Bustamante, C., Macosko, J. C. & Wuite, G. J. L. (2000) *Nature Reviews Mol. Cell Biol.* **1,** 130-136.
9. Clausen-Schaumann, H., Seitz, M., Krautbauer, R. & Gaub, H. E. (2000) *Curr. Opin. Chem. Biol.* **4,** 524-530.
10. Noy, A., Vezenov, D. & Lieber, C. (1997) *Ann. Rev. Mat. Sci.* **27,** 381-421.
11. Moy, V. T., Florin, E. L. & Gaub, H. E. (1994) *Science* **266,** 257-9.
12. Evans, E. & Ritchie, K. (1997) *Biophys. J.* **72,** 1541-1555.
13. Albrecht, H., Burke, P. A., Natarajan, A., Xiong, C.-Y., Kalicinsky, M., DeNardo, G. L. & DeNardo, S. J. (2004) *Bioconjugate Chem.* **15,** 16-26.
14. Brayman, M., Thathiah, A. & Carson, D. D. (2004) *Reprod Biol Endocrinol* **2,** 4.
15. O'Connor, J. C., Julian, J., Lim, S. D. & Carson, D. D. (2004) *Prostate Cancer and Prostatic Diseases,* 1-9.
16. Gendler, S. J. & Spicer, A. P. (1995) *Annu Rev Physiol.* **57,** 607-634.
17. Schut, I. C., Waterfall, P. M., Ross, M., O'Sullivan, C., Miller, W. R., Habib, F. K. & bayne, C. W. (2003) *British J. Urol. Int.* **91,** 278-283.
18. Schut, I., Waterfall, P., Ross, M., O'Sullivan, C., Miller, W., Habib, F. & Bayne, C. (2003) *British J. Urol. Int.* **91,** 278-283.
19. Richman, C. M. & DeNardo, S. J. (2001) *Crit. Rev. Onco./Hemato.* **38,** 25-35.
20. DeNardo, S. J., DeNardo, G. L., Yuan, A., Richman, C. M., O'Donnell, R. T., Lara, P. N., Kukis, D. L., Natarajan, A., Lamborn, K. R., Jacobs, F. & Siantar, C. L. H. (2003) *Clin. Cancer Res.* **9,** 3938S-3944.
21. Winthrop, M. D., DeNardo, S. J., Albrecht, H., Mirick, G. R., Kroger, L. A., Lamborn, K. R., Venclovas, C., Colvin, M. E., Burke, P. A. & DeNardo, G. L. (2003) *Clin. Cancer Res.* **9,** 3845S-3853.
22. Fontenot, J. D., Tjandra, N., Bu, D., Ho, C. & Montelaro, R. C. (1993) *Cancer Res.* **53,** 5386-5394.
23. Fontenot, J. D., Finn, O. J., Dales, N., Andrews, P. C. & Montelaro, R. C. (1993) *Peptide Res.* **6,** 330-336.
24. Albrecht, H., Burke, P. A., Natarajan, A., Xiong, C. Y., Kalicinsky, M., DeNardo, G. L. & DeNardo, S. J. (2004) *Bioconjug. Chem.* **15,** 16-26.
25. Butt, H. J. & Jaschke, M. (1995) *Nanotechnology* **6,** 1-7.
26. Oesterhelt, F., Rief, M. & Gaub, H. E. (1999) *New J. Phys.* **1,** 1-11.

27. Boehm, M. K., Corper, A. L., Wan, T., Sohi, M. K., Sutton, B. J., Thornton, J. D., Keep, P. A., Chester, K. A., Begent, R. H. J., Perkins, S. J. (2000) *Biochem. J.* **346,** 519-528.
28. Thompson, J. D., Higgins, D. G., Gibson, T. J. (1994) *Nucleic Acids Res.* **22,** 4673-4680.
29. Sali, A., and Blundell, T. L. (1993) *J. Mol. Biol.* **234,** 779-815.
30. Sippl, M. J. (1993) *Proteins* **17,** 355-362.
31. Dokurno, P., Bates, P. A., Band, H. A., Stewart, L. M. D., Lally, J. M., Burchell, J. M., Taylor-Papadimitriou, J., Snary, D., Sternberg, M. J. E., Freemeont, P. S. (1998) *J. Mol. Biol.* **284,** 713-728.
32. Morris, G. M., Goodsell, D. S., Halliday, R. S., Huey, R., Hart, W. E., Belew, R. K., Olson, A. J. (1998) *J. Comput. Chem.* **19,** 1639-1662.
33. Fontenot, J., Mariappan, S., Catasti, P., N, D., Finn, O. & Gupta, G. (1995) *J Biomol Struct Dyn.* **13,** 245-260.
34. Weiner, S. J., Kollman, P. A., Case, D. A., Singh, U. C., Ghio, C., Alagona, G., Profeta, S., Weiner, P. (1984) *J. Am. Chem. Soc.* **106,** 765-784.
35. Legge, G. B., Morris, G. M., Sanner, M. F., Takada, Y., Olson, A. J., Grynszpan, F. (2002) *Proteins: Struc. Func. Genetics* **48,** 151-160.
36. Florin, E. L., Moy, V. T. & Gaub, H. E. (1994) *Science* **264,** 415-17.
37. Ratto, T. V., Langry, K. C., Rudd, R. E., Balhorn, R. & McElfresh, M. (2004) *Biophys. J.* **86,** 322A.
38. Kienberger, F., Pastushenko, V., Kada, G., Gruber, H., Riener, C., Schindler, H. & Hinterdorfer, P. (2000) *Single Molecules* **1,** 123-128.
39. Evans, E. (1999) *Faraday Discuss. Chem. Soc.* **111,** 1-16.
40. Evans, E. & Ritchie, K. (1997) *Biophys. J.* **72,** 1541-1555.
41. Bell, G. I. (1978) *Science* **200,** 618-627.
42. Friedsam, C., Wehle, A. K., Kuhner, F. & Gaub, H. E. (2003) *J. Phys.-Cond. Matt.* **15,** S1709-S1723.
43. Evans, E. (2001) *Ann. Rev. Biophys. Biomol. Struct.* **30,** 105-128.
44. Hammer, D. & Apte, S. (1992) *Biophys J* **63,** 35-57.
45. Williams, P. M. (2003) *Analytica Chim. Acta* **479,** 107-115.
46. Evans, E. & Williams, P. (2002) in *Physics of Bio-Molecules and Cells*, eds. Flyvbjerg, H., Jülicher, F., Ormos, P. & David, F. (Springer and EDP Sciences, Heidelberg), Vol. 75, pp. 187-203.
47. Strunz, T., Oroszlan, K., Schafer, R. & Guntherodt, H. J. (1999) *Proc. Nat. Acad. Sci. USA* **96,** 11277-11282.
48. Seifert, U. (2000) *Phys. Rev. Lett.* **84,** 2750-2753.
49. Tees, D. F. J., Woodward, J. T. & Hammer, D. A. (2001) *J. Chem. Phys.* **114,** 7483-7496.
50. Masunov, A., Lazaridis, T. (2003) *J. Am. Chem. Soc.* **125,** 1722-1730.
51. Gruia, A. D., Fischer, S. & Smith, J. C. (2004) *Chem. Phys. Lett.* **385,** 337-340.

FIGURE CAPTIONS:

Figure 1: A. Schematic of a multivalent radioimmunotherapeutic agent interacting with the target receptor on the surface of a cancer cell. Flexible tethers link the targeting antibodies to the radioactive payload. **B**. Schematic of the force spectroscopy measurement showing the AFM tip connected to an antibody and a sample surface connected to the target MUC1 peptide with flexible PEG tethers. **C**. A representative force vs. probe-sample separation trace showing different interaction regions (see the main text for explanation of the regions). The blue line indicates an extended Freely Jointed Chain model fit for the tether stretching event.

Figure 2: A. Histograms of the rupture forces measured in a one linker length rupture region (blue filled bars) and two linker lengths rupture region (red unfilled bars). An arrow indicates the peak corresponding to the specific MUC1-antibody interactions. **B.** Histograms of the rupture forces obtained in the two-tether lengths region in absence (red unfilled bars) and in presence (blue filled bars) of the excess of MUC1 in solution.

Figure 3: A-C. Individual tether stretch traces before specific bond rupture events showing a single bond rupture (**A**) and two consecutive bond ruptures in quick succession (**B,C**). Blue lines indicate extended FJC model fits for each of the rupture traces. The pauses between two rupture events were 2 ms (**B**) and 15 ms (**C**). **D.** Dynamic force spectra for single bond rupture (□) and stepwise bond rupture (◊). The loading rate for the stepwise bond rupture was normalized by the number of bonds being loaded. Solid lines show the fits of each spectrum to Eq. 1.

Figure 4: A. Dynamic force spectra for the rupture of one (□), two (◊), and three (∇) MUC1-antibody bonds. The loading rates for the multi-bond rupture events were normalized by the number of bonds. Solid lines represent the best fits of each spectrum to the Eq. 1. **B-D**. Histograms of normalized residuals from A for one (**B**), two (**C**), and three (**D**) bonds. The residuals were normalized by the corresponding value of the force scale f_β, Solid lines are Gaussian fits with the width of 1, 2, and 3, respectively.

Figure 5. A comparison of the normalized dynamic force spectra for the rupture of one (□), two (◊), and three (∇) MUC1-antibody bonds with the prediction of the uncorrelated multiple bond rupture model. The experimental data were normalized according to the Eq. 3. Note that for this plot the loading rate was *not* normalized by the number of bonds (unlike the data on Figure 5**A**). Solid lines represent the results of the numerical solutions of the kinetic equations 4 and 5 for N=1 (-♦-), 2 (-▼-), and 3 (-▲-). (χ^2 values for the correlation between the experimental data and the model correspond to the probability of null hypothesis of $p<10^{-6}$ for one and two bonds and $p<2\cdot10^{-6}$ for three bonds.)

Figure 6: Homology model simulation results. **A.** The lowest energy docked MUC1 fragment onto the surface of the CD5 homology model. The Asp of MUC1 is oriented into a pocket on the surface of CD5. **B.** A close-up of the interaction between Asp of MUC1 and residues within the antibody. **C.** Close up of the MUC1 fragment bound on the scFv surface.

Table 1: The distances to the transitions state, x_β, kinetic off-rates, k_{off}, and the average bond lifetime $\tau_{off}=1/k_{off}$ values determined from the fits of the data on the Figure 6 to the Eq. 1.

	1 Bond	**1 Bond, stepwise**	**2 Bonds**	**3 Bonds**
χ_β ,Å	2.8±0.2	2.7±0.3	2.0±0.4	2.4±1.5
k_{off} ,s^{-1}	$2.6x10^{-3}$	$6.9x10^{-3}$ s^{-1}	$7.2x10^{-5}$ s^{-1}	$3.6x10^{-8}$
τ_{off}	284 sec	144 sec	3.8 hrs	320 days

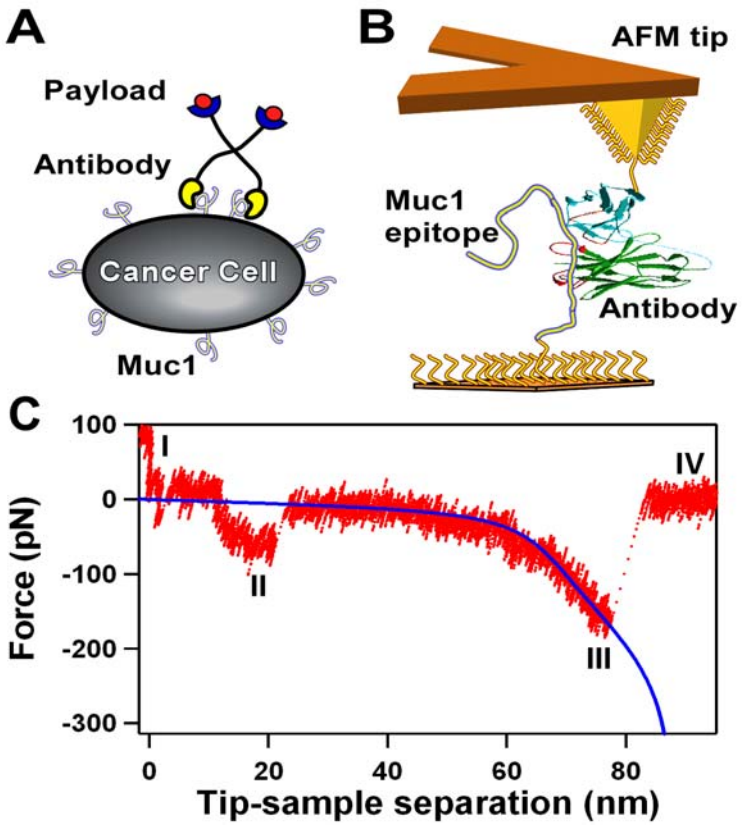
A
Payload
Antibody
Cancer Cell
Muc1
B
AFM tip
Muc1
epitope
Antibody
C
Force (pN)
100
0
-100
-200
-300
I
II
III
IV
0
20
40
60
80
Tip-sample separation (nm)

FIGURE 1

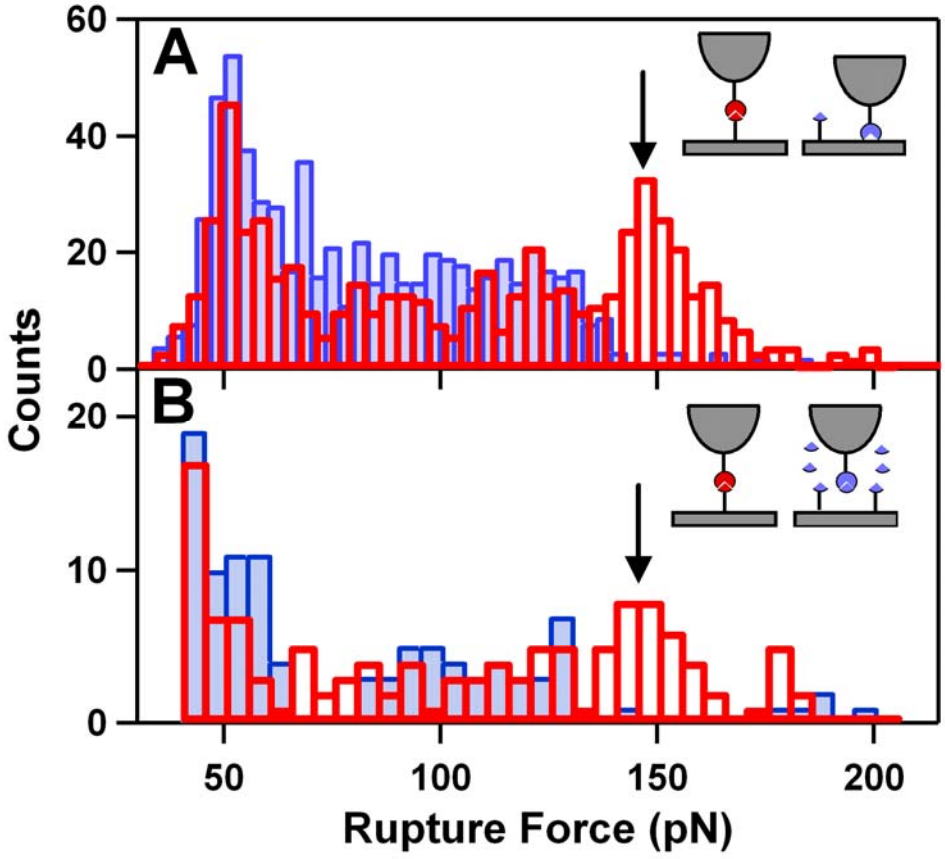

FIGURE 2

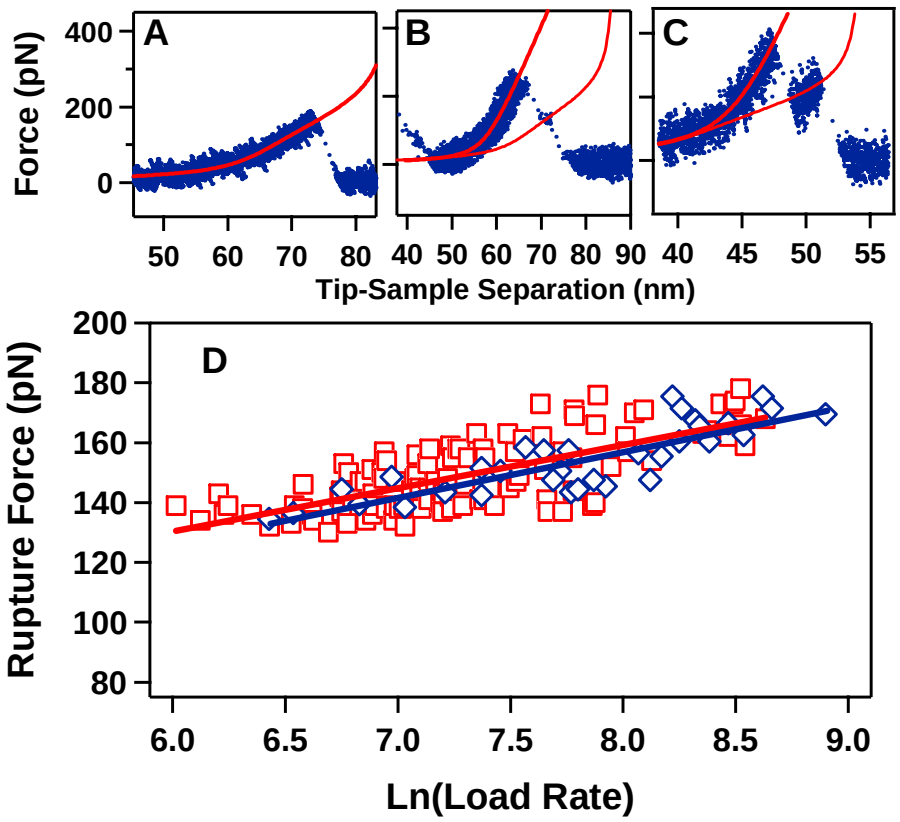
A
B
C
D
Force (pN)
400
200
0
50
60
70
80
40
50
60
70
80
90
40
45
50
55
Tip-Sample Separation (nm)
Rupture Force (pN)
200
180
160
140
120
100
80
6.0
6.5
7.0
7.5
8.0
8.5
9.0
Ln(Load Rate)

FIGURE 3

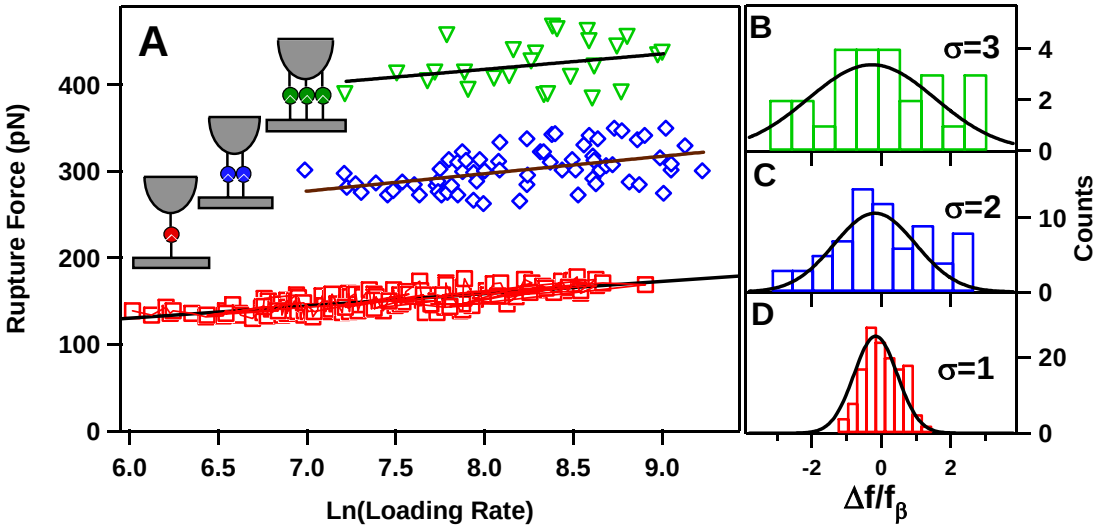
A
B
C
D
σ=3
σ=2
σ=1
Rupture Force (pN)
Ln(Loading Rate)
Counts
Δf/f$_\beta$
0
100
200
300
400
6.0
6.5
7.0
7.5
8.0
8.5
9.0
-2
0
2
4
10
20

FIGURE 4

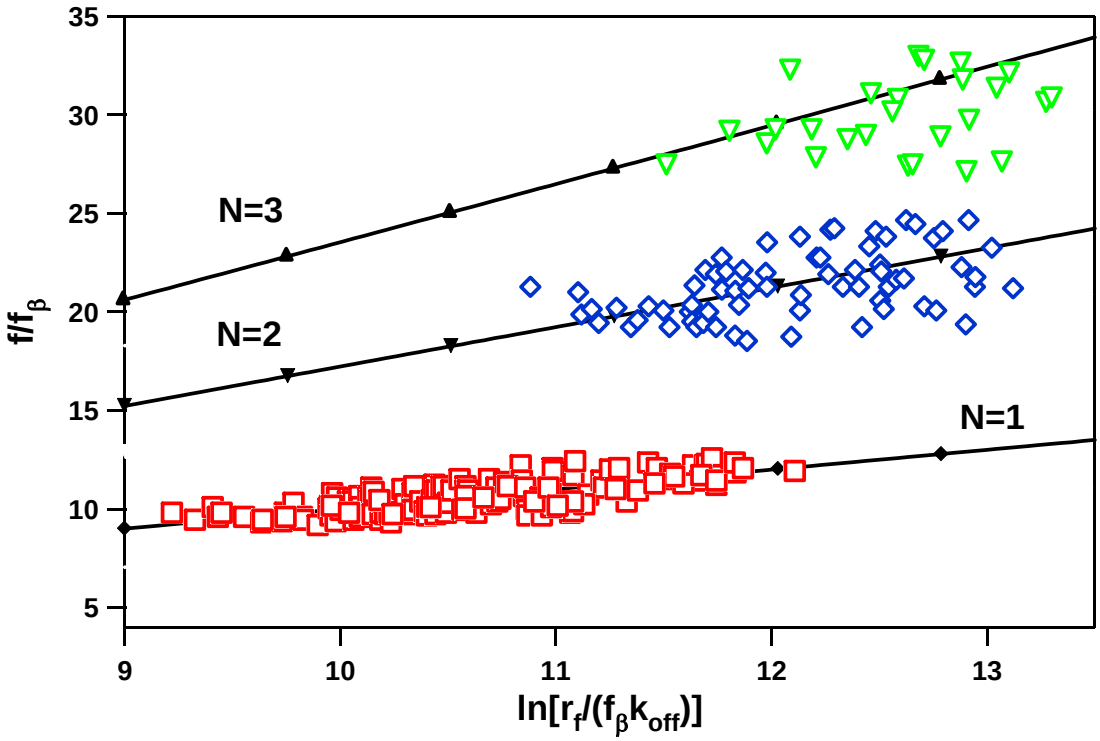

FIGURE 5

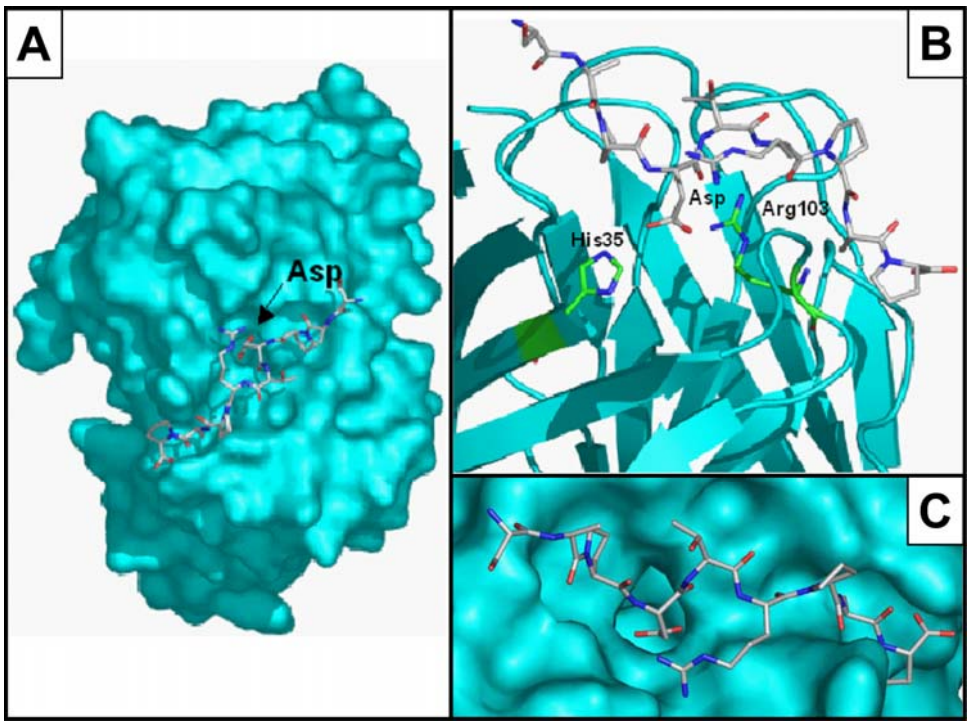

FIGURE 6